Shock Propagation in Aerogel and TPP Foams for Inertial Fusion Energy Target Design

C. Parisuaña,[1,2,3,4] M. P. Valdivia,[5] V. Bouffetier,[6] K. Kurzer-Ogul,[4,7] G. Pérez-Callejo,[8] S. Bott-Suzuki,[5] A. Casner,[9] N. S. Christiansen,[4] N. Czapla,[1] D. Eder,[10] E. Galtier,[1] S. H. Glenzer,[1] T. Goudal,[9] B. M. Haines,[4] D. Hodge,[2,11] M. Ikeya,[1] L. Izquierdo,[12] D. Khaghani,[1] Y. Kim,[4] S. Klein,[13] A. Koniges,[14] H. J. Lee,[1] M. Leininger,[2,11] A. F. T. Leong,[4] R. S. Lester,[4] M. Makita,[15] D. Mancelli,[16,17,18] W. M. Martin,[2,1,19] B. Nagler,[1] R. L. Sandberg,[2,11] A. Truong,[20] M. Vescovi,[21] A. E. Gleason,[2,1] and P. M. Kozlowski[4]

[1)]*SLAC National Accelerator Laboratory, Menlo Park, California 94025, USA*
[2)]*DOE IFE-STAR RISE-hub, Fort Collins, CO 80523, USA*
[3)]*Department of Mechanical Engineering, Stanford University, Stanford, California 94305, USA*
[4)]*Los Alamos National Laboratory, Los Alamos, New Mexico, 87545, USA*
[5)]*Center for Energy Research, University of California San Diego, San Diego, California 92093, USA*
[6)]*CELLS-ALBA Synchrotron Light Source, Barcelona, Spain*
[7)]*University of Rochester, Department of Mechanical Engineering, Rochester, New York, USA*
[8)]*Departamento de Física Teórica Atómica y Óptica, Universidad de Valladolid, 47011 Valladolid, Spain*
[9)]*CEA, DAM, DIF, Arpajon, France*
[10)]*Physics and Astronomy, University of Hawai'i at Mānoa Honolulu, HI, USA*
[11)]*Department of Physics and Astronomy, Brigham Young University, Provo, Utah 84602, USA*
[12)]*Instituto de Física, Pontificia Universidad Católica de Chile, Santiago 7820436, Chile*
[13)]*University of Michigan, Ann Arbor, Michigan, USA*
[14)]*Information and Computer Sciences, University of Hawai'i at Mānoa, Honolulu, HI, USA*
[15)]*European XFEL, Schenefeld, Germany*
[16)]*Institute of Plasma Physics & Lasers, University Research & Innovation Centre, Hellenic Mediterranean University, Rethymno, Crete, Greece*
[17)]*Department of Electronic Engineering, School of Engineering, Hellenic Mediterranean University, Chania, Crete, Greece*
[18)]*University of Bordeaux, CNRS, CEA, CELIA, Talence, France*
[19)]*Physics Department, Stanford University, Stanford, California 94305, USA*
[20)]*Department of Mechanical and Aerospace Engineering, University of California San Diego, La Jolla, California 92093, USA*
[21)]*Helmholtz-Zentrum Dresden-Rossendorf (HZDR), Dresden, Germany*

(*Corresponding Author: aegleaso@slac.stanford.edu)

(Dated: 12 June 2025)

Achieving practical inertial fusion energy (IFE) requires the development of target designs with well-characterized microstructure and compression response. We measured shock dynamics in low-density (17.5-500 $\mathrm{mg/cm^3}$) aerogel and two-photon polymerization (TPP) foams using X-ray phase contrast imaging (XPCI) methods and Velocity Interferometer System for Any Reflector (VISAR). By analyzing shock front evolution, we examined how target type and density influence shock propagation and energy dissipation. Talbot-XPCI shows that aerogels support a smooth, bowed shock front due to their homogeneous nanometer-scale pore network. In contrast, TPP foams exhibit irregular, stepwise propagation driven by interactions with their periodic micron-scale lattice. Shock velocity follows a power-law relation: aerogels deviate from classical $\rho^{-1/2}$ scaling due to pore-collapse dissipation, while TPP foams follow the trend with larger uncertainties from density variations. Comparisons with xRAGE simulations reveal systematic underestimation of shock speeds. These results provide the first experimental constraints on shock propagation in TPP foams over a wide density range and highlight the influence of internal structure on anisotropic shock behavior. Our findings support improved benchmarking of EOS and hydrodynamic models and inform the design of foam architectures that promote implosion symmetry in IFE capsules.

I. INTRODUCTION

The achievement of ignition at the National Ignition Facility (NIF)[1–3] marked a pivotal moment in inertial fusion energy (IFE) research, demonstrating energy gain feasibility using inertial confinement fusion (ICF).[2,4] However, realizing the goal of practical fusion energy requires a deeper understanding of target physics with the development of advanced diagnostic capabilities to analyze material behavior under extreme conditions.[5,6] A future IFE plant demands target designs enabling production at high manufacturing rates to support high-repetition-rate operations (∼10-20 Hz), a cadence necessary for commercial fusion energy applications.[7,8] The precision required for cryogenic NIF targets, such as submicron uniformity and micron-scale fill tubes to mitigate jetting, presents substantial challenges for rapid manufacturing.[4] Acquiring high-quality experimental data under extreme conditions is essential to validate simulations and refine target designs for scalable production.[5,9]

In addition to target microstructure, the performance of an IFE capsule depends critically on the fraction of laser energy that is converted into the initial ablation pressure (P_{abl}), known as drive coupling.[5,10] Future drivers for IFE power plants will fire at high repetition rates (∼ 10–20 Hz) with pulses in the

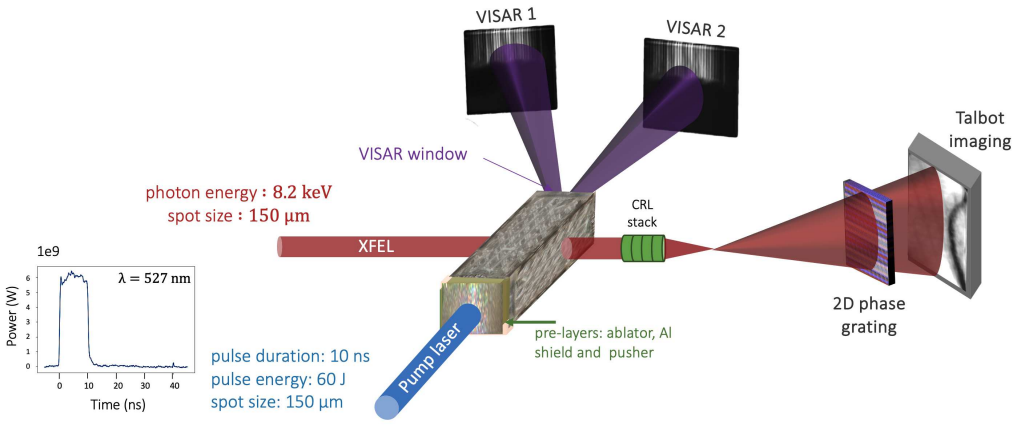

FIG. 1. Schematic of the experimental setup at MEC for simultaneous VISAR and Talbot X-ray phase contrast imaging. A pump laser ($\lambda = 527\,\text{nm}$) delivers $\sim 60\,\text{J}$ of energy in a 150 µm spot size on target, over a 10 ns duration to drive a shock through foam targets. The VISAR diagnostic provides time-resolved measurements of breakout times, while Talbot-XPCI captures density gradients and structural evolution in the shocked foam.

kilojoule range, a stark contrast to today's megajoule-class, single-shot facilities like NIF.[11] To achieve the same implosion pressures with three orders of magnitude less energy, the specific coupling ($\text{GPa}\,\text{kJ}^{-1}$) must increase substantially.[10] Low-density foams offer an ideal platform to explore this scaling because their porosity influences volumetric absorption and the efficiency with which the generated pressure is transferred. Hence, measuring shock velocity and front morphology in foams provides a macroscopic proxy for driver-coupling efficiency under IFE-relevant conditions and guides the interpretation of subsequent target response.

In this context, deuterium–tritium (DT) wetted foam capsules have emerged as promising alternatives to traditional solid-layered DT targets in ICF experiments.[12,13] Their porous microstructures enhance robustness against hydrodynamic instabilities by promoting more uniform shock propagation and reducing interface mixing during implosions.[9] This behavior is consistent with earlier work by Sacks and Darling,[13] who proposed that small pore size, low-density foams [14] can passively stabilize DT layers against gravitational slumping and hydrodynamic distortions during implosion.[13] These foam-based targets can be manufactured more rapidly with fewer precision constraints, offering a viable path for scaling to high-repetition-rate fusion facilities.[13,15]

Micro and nanofabrication using two photon polymerization (TPP), also known as two-photon lithography (TPL), is relatively new.[16] These methods enable custom-tailored microarchitectures for specific bulk densities and gradient profiles, which may improve energy absorption and optimize shock compression dynamics.[17–19] Recent advancements in projection-based parallelized printing with ultrafast lasers offer new pathways to economically scale TPP target production efficiency for IFE.[16,20]

The use of TPP printed lattices in high-energy density (HED) experiments is even more recent, reflected by the scarcity of experimental measurements.[15,17–19,21–23] The complex morphology of these targets results in Attwood number variations for the many interfaces encountered, which can generate transmitted and reflected waves interacting with each other. Furthermore, modeling these targets can be challenging, as they are not necessarily symmetric, computationally-intensive 3D simulations are required. Despite these challenges, TPP printed lattices hold great promise for IFE with the ability to tailor targets with precisely manufactured structures, unlike their chemically synthesized counterparts.

This study leverages Talbot diagnostic techniques for X-ray phase contrast imaging (XPCI) and the Velocity Interferometer System for Any Reflector (VISAR) to investigate shock dynamics in porous foams. Aerogel targets are used as a well-established benchmark[24–36] before extending the analysis to TPP lattice foams. Talbot images can track shock front evolution with high diagnostic sensitivity, resolving the density gradients and mesoscale interactions within the foam structure[37]. VISAR diagnostics provide precise breakout time measurements to estimate shock velocity. In concert with hydrodynamic simulations, we determine microstructure influence (e.g., engineered porosity) in shock propagation, providing critical insights for advanced target design. These studies underscore the need to refine models by incorporating lattice-driven shock dynamics. Our results showcase TPP lattices as a promising platform for IFE target development, offering a new level of control over density and structural uniformity

compared to conventional foams, which is crucial for maintaining energy coupling and hydrodynamic stability throughout the implosion process.

The remainder of this paper is organized as follows. In Section II we describe our experimental configuration, including target fabrication (aerogel and TPP foams), the pre-layer stack, the Talbot X-ray phase-contrast imaging (XPCI) diagnostic setup, and the VISAR breakout-time measurements. Section III presents the shock-front evolution observed by Talbot-XPCI and VISAR, quantifies shock velocities across foam densities, and compares these data with xRAGE hydrodynamic simulations. In Section IV we discuss key findings: the macroscopic signatures of driver coupling in low-density foams, deviations from the ideal $\rho^{-1/2}$ scaling due to energy-dissipative pore collapse, and the distinct lattice-driven perturbations in TPP foams. Finally, Section V summarizes our conclusions and outlines future directions for refining driver-coupling models and extending these diagnostics to IFE target development.

II. METHODS

A. Experimental Setup

The experimental setup is shown in Figure 1. At the Linac Coherent Light Source (LCLS) facility, foam samples were driven by the Matter in Extreme Conditions (MEC) long-pulse laser.[38] A 10 ns flat-top pulse delivered an average of (61.74 ± 3.02) J per shot, with energies ranging from 51.01 J to 68.31 J. The beam was focused to a 150 µm spot size on target with estimated intensity of $\sim 3.4 \times 10^{13}$ W/cm^2. Foams bulk density ranged from 17.5 mg/cm^3 to 500 mg/cm^3, with a 300 µm width, and 300 or 500 µm length. The sample set included aerogel (porous) foams and TPP polymer struts in a simple cubic lattice design. The aerogel foams exhibit expected pore size on the order of tens of nanometers ($\sim 50 \pm 20$ nm). For TPP targets, bulk density was controlled through strut thickness variation and limited by 3D printing capabilities (3-4 µm). Thus, significant variations were expected for the lowest nominal densities. Microscope metrology was conducted to estimate bulk density for each TPP target from strut thickness measurements. To maintain consistency in our dataset, we excluded TPP foams that deviated by more than 2σ from the average density within a given target batch:

$$|\rho_i - \bar{\rho}| > 2\sigma$$

where $\bar{\rho}$ is the mean density of the batch and σ is the standard deviation of the density distribution.

Each full target assembly consisted of three pre-layers on the side facing the drive laser: an ablator, an aluminum shield, and a pusher layer of ∼60-80 µm total thickness. A high-energy shock wave was generated by irradiating the target axially, reaching ablation pressures of ∼250-350 GPa (as seen in our xRAGE simulations). The pre-layer structure differed between aerogel and TPP targets and was consistent within target type.

B. Shock Front Evolution from Talbot X-ray Phase Contrast

X-ray Phase Contrast Imaging is a common diagnostic tool in high-energy-density physics (HEDP).[33,39–41] It is an imaging method which makes use of the phase shift imposed on a wave front as it travels through an inhomogeneous medium.[33,42] Shock waves result in a rapid change in density and are ideal target for this diagnostic and they have already been extensively studied using standard absorption radiography.[43–47] The Talbot-XPCI diagnostic in our experiment follows principles similar to those used in HEDP applications as discussed by Valdivia et al.[48–50] Our setup leverages the LCLS X-ray free electron laser brilliance coupled with a long pulse (10 ns) laser present at the MEC with the MEC X-ray Imaging (MXI) instrument[51,52] to image and locate shock front positions in both TPP and aerogel low-density foams, with higher accuracy compared to standard absorption-based radiography,[34] and better resolution compared to previous XPCI experiments.[33,40] We generated the Talbot XPCI images using the Talbot Interferometry Analyzer and Numerical Tool (TIA/TNT) code developed by Pérez-Callejo et al.[53,54]

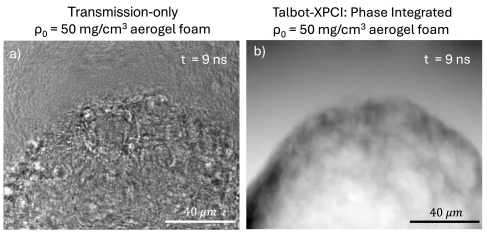

FIG. 2. Talbot XPCI of 50 mg/cm^3 aerogel foam during shock compression.[53] (a) Transmission-only radiograph. (b) Talbot-XPCI phase-integrated map using TIA/TNT post-processed[53] shows a single, gently curved shock front that spans the full field of view as a bright-to-dark transition with almost no lateral corrugation. Ahead of it, the unshocked aerogel remains nearly featureless, while the region behind the front darkens uniformly. The front's continuity indicates that the interconnected, sub-micron pore network offers a nearly homogeneous impedance, so the shock advances as a smooth, quasi-planar (bow-shaped) surface with only minor, long-wavelength curvature set by the drive geometry.

C. Breakout time measurements using Velocity Interferometer System for Any Reflector (VISAR) Diagnostics

We employed a dual VISAR interferometer setup, with each VISAR viewing the rear side of the target. A window was attached to the rear of the foam targets to ensure high-fidelity reflection of the probe laser beam for precise breakout time measurements. The dual VISAR configuration provided redundancy and enabled independent breakout time determination for each shot.

Aerogel (500 µm)		**Aerogel** (300 µm)		**TPP** (300 µm)	
Density (mg/cm^3)	**VISAR shots**	**Density** (mg/cm^3)	**VISAR shots**	**Density** (mg/cm^3)	**VISAR shots**
20	4	20	2	17.5	1
50	10	50	1	35	3
100	4	100	0	70	2
250	5	250	0	105	3
500	3	500	0	-	-

TABLE I. Number of VISAR shots per target type and density. The table summarizes the number of VISAR measurements obtained for each target category: aerogel foams (500 µm and 300 µm lengths) and TPP lattice foams (300 µm). Each shot is counted only once, despite the fact that two VISAR breakout times were recorded per shot.

The VISARs produced fringe patterns, as shown in Figure 3. However, no fringe motion was observed, preventing us from using impedance matching for direct shock velocity measurements using Doppler shift. Instead, we determined shock breakout times by processing raw VISAR data and applying calibration corrections to subtract t_0. Each shot yielded two breakout times, which were then used to estimate the shock velocity. To obtain exclusively the shock speed of the foam, we subtracted the transit time of the shock in the pre-layer region.

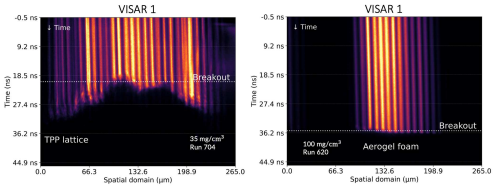

FIG. 3. VISAR images showing shock breakout for (left) a 35 mg/cm^3 TPP lattice foam and (right) 100 mg/cm^3 aerogel foam.

Shock breakout times were determined using fringe phase analysis with the Fourier transform method described in[55]. No rear window was used on our target configuration. Consequently, we do not observe fringe motion, which would be expected if a window were present. Instead, the diagnostic signal consists of continuous fringe visibility, followed by an abrupt loss of reflectivity when the shock reaches the rear surface. This loss of reflectivity is used as a surrogate for shock breakout. As shown in Figure 3, aerogel foams exhibited uniform breakout patterns, whereas TPP lattices displayed irregular, modulated fringe behavior. To account for this, the earliest observed breakout time was defined as the breakout time, marking the first detectable shock arrival at the rear surface of the target. This method provided a robust and consistent approach for estimating shock velocities across foam densities, even in the absence of continuous fringe motion.

D. Complementarity of VISAR and Talbot Imaging

The integration of VISAR and Talbot X-ray phase contrast imaging provides a comprehensive diagnostic framework for examining shock propagation in foam materials. While VISAR measures breakout times at the target's rear surface, Talbot imaging enabled tracking of the shock front position at discrete time intervals. Therefore, VISAR shock speeds at breakout is an average over all phases of the shock development, while Talbot-XPCI offer an instantaneous shock position measurement of the shock.

This complementary approach is particularly valuable as it allows us to probe shock front dynamics at different stages: while the drive laser is on, after the laser is turned off, and as the shock reaches the rear of the target. By capturing the shock evolution at multiple points in time, we can assess whether localized structural features from target manufacturing —detected early in the Talbot-XPCI images- persist and influence the overall shock front development at later stages, ultimately affecting VISAR fringe patterns at breakout.

III. RESULTS

A. Shock front position as a function of time using Talbot X-ray Phase Contrast Imaging

Shock front positions for aerogel foams, measured using Talbot-XPCI, are shown in Figure 4. The data reveal the ballistic phase of shock propagation, consistent with previous experiments by Rigon et al.[24] on aerogel foams of similar densities. Their study describes this initial phase as being dominated by the ablator-shield-pusher system until a sufficient mass of foam is swept by the shock.[24] As a result, higher-density foams begin to decelerate earlier than lower-density foams.

At early times, the shock dynamics are indistinguishable across different foam densities, as they are primarily governed by the pre-layer region rather than the foam itself.[24] The transition to the second phase, where the shock starts decelerating, is evident in Figure 5. In this phase, the differences in shock dynamics across densities become more pronounced. The rate of deceleration increases with foam density, as demonstrated by the variation in shock arrival times at the rear of the target, as observed in VISAR breakout times also seen in Figure 5.

Figure 4 also includes xRAGE simulations for the shock front positions in aerogel foams across all tested densities. At early times ($\leq$ 3.9 ns), the shock, generated by the drive laser at the target's front surface, propagates at the same velocity for all densities. This behavior is expected since all targets share the same ablator, shield, and pusher layers. Beyond this time, lower-density foams are expected to sustain higher shock speeds, as indicated by the solid lines representing xRAGE simulation results. The experimental data show that xRAGE simulations systematically underestimate the shock velocity.

Dashed lines in Figure 4 represent the best linear fits to the experimental data. A linear fit was chosen under the assump-

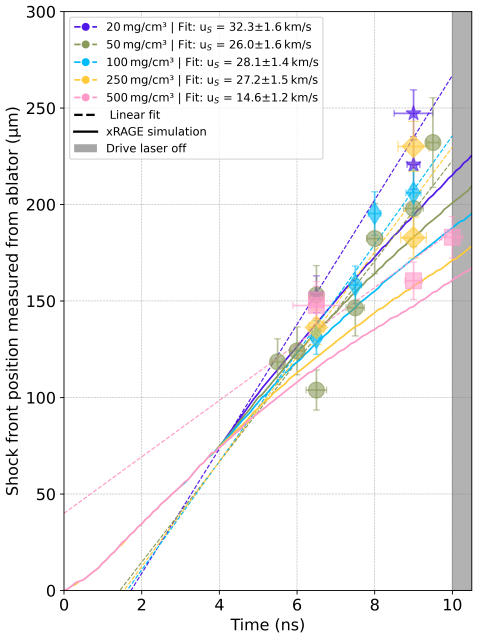

FIG. 4. Shock front position as a function of time for aerogel foams of initial densities 20, 50, 100, 250 and 500 mg/cm^3 under shock compression. Filled colored markers show Talbot–XPCI measurements (vertical error bars reflect uncertainties in both time and shock front position measurements; horizontal error bars reflect foam-thickness variation), the gray region marks the period after the drive laser is switched off. Dashed colored lines show linear least-squares fits to the data, constrained using the xRAGE-predicted ablator transit time and an ablator stack thickness between 60–90μm. Solid colored lines correspond to xRAGE hydrodynamic simulations. In all cases, the simulations systematically underpredict the experimentally measured shock velocities.

tion that, while the drive laser sustains the shock, it should maintain a relatively constant speed. The shock speeds extracted from these fits are consistent within error for all densities, except for the 500 mg/cm^3 foam, which exhibits a lower velocity. The measured shock speeds reported here are consistent with previous studies, including the results of Rigon et al. (20 mg/cm^3 - 500 mg/cm^3)[24] and Antonelli et al. for (100 mg/cm^3) foams.[33].

A more detailed analysis of shock dynamics could be performed by leveraging Talbot-XPCI to extract instantaneous shock velocities, thereby relaxing the assumption of constant speed while the laser is driving the shock. While such an analysis is beyond the scope of this paper, it will be addressed in future studies. We report in Table II the corresponding particle velocity (Up), pressure, and density ratio $\frac{\rho}{\rho_0}$ for the fitted aerogel shock speeds. These estimated values were computed using SESAME tables.

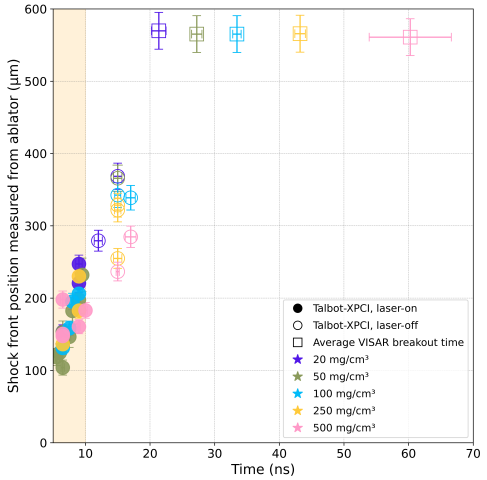

FIG. 5. Shock front position as a function of time for different aerogel foam densities after driving laser is off using Talbot-XPCI and VISAR breakout times. Talbot-XPCI combined with VISAR breakout times show deceleration for all foam densities at later times.

Initial density ρ_0 (mg/cm^3)	u_s (km/s) 3.9 ns $\leq t \leq$ 10 ns	P (GPa)	u_p (km/s)	ρ/ρ_0
20	32.3 ± 1.6	17.82 ± 1.77	27.61 ± 1.38	6.89 ± 1.03
50	26.01 ± 1.6	28.31 ± 3.52	21.86 ± 1.36	6.27 ± 0.94
100	28.10 ± 1.4	65.12 ± 6.57	23.26 ± 1.18	5.81 ± 0.58
250	27.2 ± 1.5	147.95 ± 16.67	21.87 ± 1.25	5.10 ± 0.26
500	14.6 ± 1.2	79.21 ± 13.73	11.14 ± 0.97	4.22 ± 0.22

TABLE II. **Equation of state for aerogel foams using experimental shock velocity (u_s)** We report experimental shock velocity (u_s) from Figure 4 and estimates of pressure (P), particle velocity (u_p), and density ratio ρ/ρ_0 for different initial densities using SESAME material number 7387

Figure 6 presents the shock front position for TPP lattice foams, obtained using both Talbot-XPCI and the averaged VISAR breakout times per density. Compared to aerogel foams, we have fewer data points due to experimental constraints. Outliers were excluded based on delivered laser energy (beyond 1σ), strut thickness measurements obtained via optical microscopy before the experiment (beyond 2σ), and deviations in shock speed (beyond 2σ). The final dataset, after applying these selection criteria, is shown in Figure 6. At early times, the TPP foams exhibit a ballistic phase, similar to aerogel foams. However, due to their shorter length 300 μm foam and 75.44 μm - 92.72 μm pre-layers region) compared to most of the aerogels we shock compressed, the time available before the shock reaches the rear VISAR window is reduced. As a result, only the highest-density lattice foam (105 mg/cm^3) exhibits distinct measurable late dynamic.

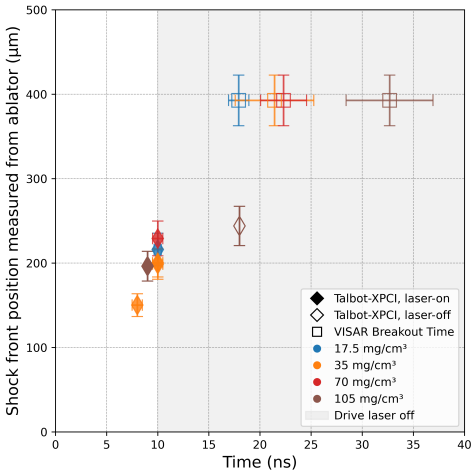

FIG. 6. Shock front position as a function of time for different TPP densities using Talbot-XPCI[53] and VISAR breakout time

.

B. Shock front morphology of aerogels and TPP lattice foams using Talbot-xray phase contrast imaging

Figure 2 compares the transmission-only image with the phase-integrated map obtained using the Talbot-XPCI TIA/TNT code.[53] The right panel of Figure 2 fully resolves the intricate structures behind the shock front when compared to transmission-only radiograph. Our findings not only corroborate that XPCI is a highly effective diagnostic for accurately determining the position of a trailing shock front[33] in low density aerogel foams, but also provide a more detailed characterization of shock front dynamics upstream and downstream.

Figure 7 presents xRAGE simulations of a 100 mg/cm^3 aerogel foam alongside the corresponding Talbot-XPCI images[53]. The simulations were run in 2D cylindrical geometry and included multigroup diffusive radiation transport, flux-limited Spitzer-Härm heat conduction, Laboratory for Laser Energetics Mazinisin laser package, a directionally-split Gudonov hydrodynamic solver[57]. The following EOS tables were used: Chamber gas SESAME 5760 (He); Al shield: SES 3720 (Al); Ablator SES 7592 (CH); Tube SES 7592 (CH); Pusher SES 7592; Foam LEOS 5110, SES 7592. The full target (ablator, shield, pusher and foam) was modeled, but does not capture purely 3D behavior.

Although the xRAGE simulation underestimates the shock speed, as shown in Figure 4, it successfully captures the overall shock morphology. Figure 7a shows density map with a non-planar, bowed shock front, an effect influenced by laser spot size on target and ablation dynamics. These density variations align with the Talbot-XPCI experimental phase map. This characteristic shock front morphology has also been previously observed by Omega experiments and simulations done by Karr et al.[56] In our case, these density gradients arise from the interaction of the polystyrene ablator, aluminum, and CH pusher as they expand into the foam before merging at later times.

Figure 7b shows a synthetic X-ray radiograph from xRAGE alongside the corresponding Talbot-XPCI Y-gradient map[53] at 7.5 ns. It is important to notice that sharp material boundaries interfaces are not explicitly resolved in the phase-contrast image (Fig. 7a.) due to phase-unwrapping limitation near high-gradient interfaces, where "infinite" refraction prevents accurate reconstruction and therefore we include here the Y-gradient map instead.

To better understand the source of the systematic underprediction of shock velocity in simulations reported in Table III, Fig. 7c shows the energy density at the foam entrance (t=3.9ns), as predicted by xRAGE, to serve as a constraint for future studies. Since all aerogel foams had identical ablator stacks, observed differences in shock velocity between experiment and simulation must be due to the material response models.

Figure 8d shows the Talbot-XPCI phase-integrated map of a 35 mg/cm^3 TPP lattice foam, capturing the spatial distribution of compressed material along the propagation axis. The bowed shock front, previously observed in aerogel foams (Figures 2 and 7), is also evident in the TPP lattice, reinforcing the conclusion that this effect arises form ablation dynamics rather than material-specific properties. The pre-shock target structure (Figure 8a) shows the internal lattice before compression, a tilted lattice foam in this case. Figure 8b shows the transmission-only image, which, due to the foam's low density, fails to capture the dynamics in both the unperturbed region ahead of the shock and the shock-compressed region behind the shock front. Unlike aerogels, Figure 8c and Figure 8d[53] sequence reveal a shock front that is highly modulated at the lattice period. In the phase-integrated map (8d), the front is broken into a series of peaks and valleys: sharp, high-gradient peaks form where the shock encounters a lattice strut, while valleys appear in the open cells. These "tooth-like" perturbations appear incipient downstream (8d)), producing alternating bands of higher and lower areal density. The result is a shock that advances in an uneven, stepwise fashion with mesoscale distortions that are entirely absent in the aerogel case, and that were also observed in their VISAR measurements (Figure 3), where variations in breakout patterns further confirm this for later times.

C. Estimation of shock speeds using VISAR breakout times

Table I shows the number of breakout time measurements for aerogels and TPP foams. Previous work[32] have used breakout times to estimate the average shock speed at the rear side of the target, providing an integrated measurement across all phases of late-stage shock development. By combining these measurements with equation of state (EOS) tables, such as SESAME, EOS values have been reported for

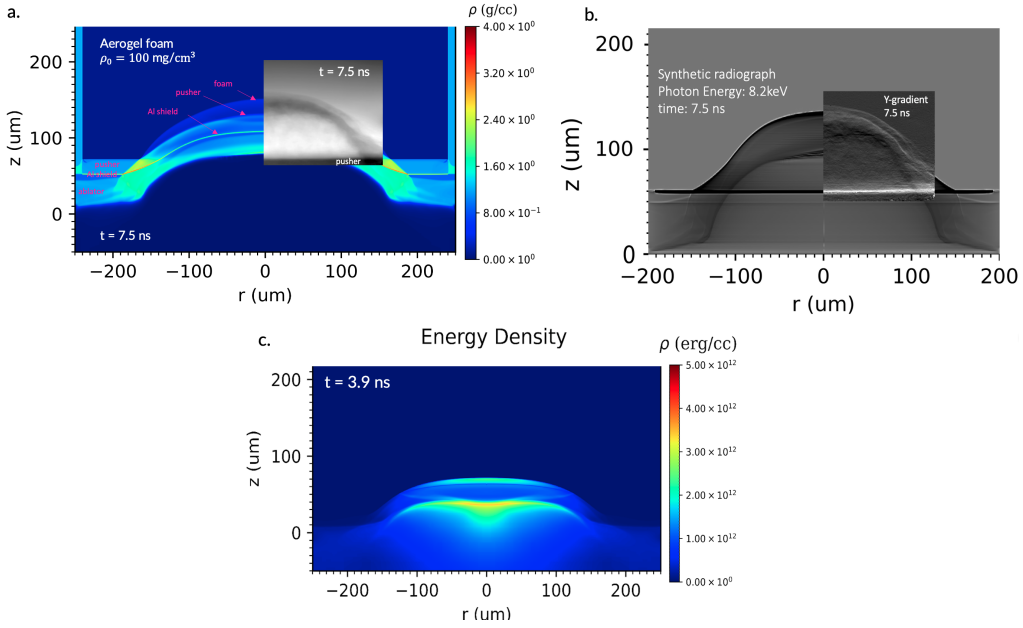

FIG. 7. Comparison of xRAGE simulation results with Talbot-XPCI experimental images for a 100 mg/cm^3 aerogel foam target. (a) Simulated 2D density map at 7.5 ns, overlaid with the Talbot-XPCI phase-integrated map[53] captured 7.5 ns after target irradiation by a square pulse that launched the shock wave. Simulation predicts a non-planar, bowed shock front structure due to laser spot size and ablation dynamics, which is consistent with the experimental Talbot-XPCI phase map. A similar shock front morphology has been reported in refraction-enhanced x-ray radiography at Omega experiments[56]. (b) Synthetic radiograph generated from the simulation at 7.5 ns, shown side by side with the experimental Y-gradient phase image.[53]. This comparison reveals strong agreement in front morphology but a mismatch in shock position. (c) Simulated energy density map at 3.9 ns, jsut before the shock enters the foam. This plot provides a constraint on the energy density delivered through the ablator-pusher stack.

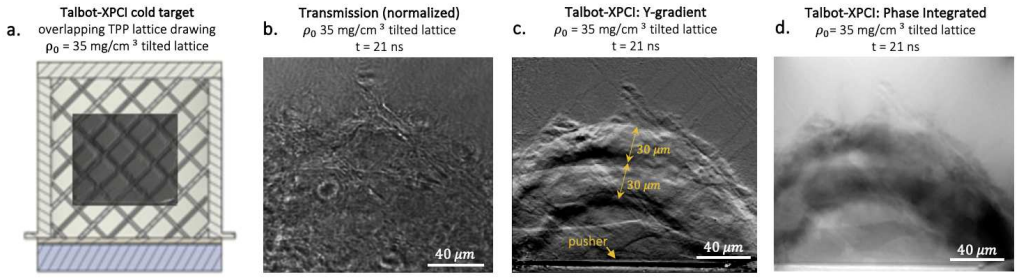

FIG. 8. **Talbot X-ray phase contrast imaging of a 35 mg/cm^3 TPP tilted lattice during a shock compression experiment using TIA/TNT post-processed images.**[53] (a) Talbot-XPCI phase integrated map of the cold target overlaid with a schematic representation, providing a scale reference for the imaged region. (b) Transmission-only radiograph following shock compression, capturing the structural evolution of the target. (c) Talbot-XPCI Y-gradient image (rads/ μm) map, highlighting variations in density gradient across the foam structure, revealing fine details of the shock front interaction with the lattice structure and compression features (± 300 nm spatial resolution). (d) Talbot-XPCI phase-integrated map showing the spatial distribution of compressed material along propagation axis, with higher densities corresponding to darker regions. The localized interactions between the shock front and the TPP lattice progressively shape the overall shock evolution, resulting in mesoscale modifications distinct from the more uniform propagation observed in aerogel Talbot-XPCI images.

low-initial-density porous foam targets (1.45–1.6 g/cm^3), enabling further exploration of the EOS plane.[32] We utilize a

similar approach here and report the estimated shock speeds (at breakout) in Figure 9 as a function of initial foam density for both target types, with error bars reflecting uncertainties in density measurements, breakout time determination, and target dimensions. Data highlight a clear trend: average shock speed decreases with increasing foam density for both aerogel and TPP lattices. This inverse relationship reflects the increased resistance of denser materials to shock propagation, as expected from fundamental shock physics.

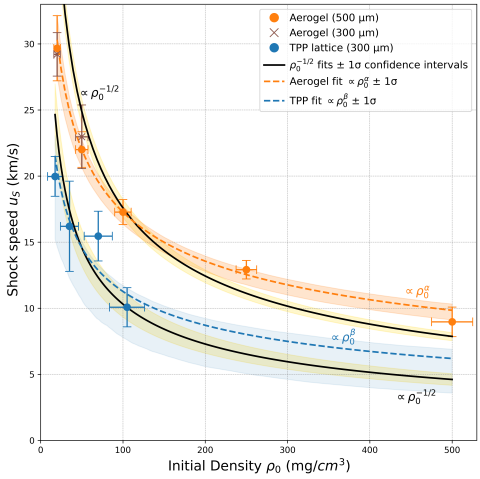

FIG. 9. Shock speed u_S as a function of initial foam density ρ_0 for TPP and aerogel targets, obtained from VISAR breakout times. Vertical error bars combine uncertainties from target length, breakout time VISAR image processing, and standard error from repeated measurements; horizontal error bars reflect strut thickness variation in TPP foams and uncertainty for aerogels. Shaded bands are the 1σ confidence intervals on each fit. Solid black curves represent theoretical scaling $u_S = A\rho_0^{-1/2}$ fit independently to each data set, with $A_{aerogel}$ = 175.9 ± 6.7 (MSE=21.2), A_{TPP} 103.10 ± 10.47 (MSE = 8.29). Dashed curves are free-exponent power-law fits $u_S = B\rho_0^{\delta}$ yielding $B_{aerogel}$ = 86.36 ± 15.7, $\alpha = -0.3494 \pm 0.0375$ (MSE = 0.26, R^2 = 0.99), B_{TPP} = (62.39 ± 34.39) $\beta = -0.3716 \pm 0.1372$ (MSE = 2.58, R^2 = 0.79)

Figure 9 compares the theoretical scaling law $U_S \propto \rho^{-1/2}$, commonly used in hydrodynamic models of porous materials, with a power-law relation of the form $U_S \propto \rho^{-\alpha}$ for both aerogel and TPP foams. The solid gold and purple curves represent the $\rho^{-1/2}$ scaling for aerogel and TPP foams, respectively, with the shaded regions indicating 1σ = 0.68% confidence band. The power-law $\rho^{-\alpha}$ fits are shown in orange and blue dashed lines for aerogel and TPP foams respectively. Aerogel and TPP foams follow the theoretical scaling law. In particular aerogel foam dataset follows closer a power-law fit, while TPP data can be described by both the theoretical and power-law relation fit within error bars.

Density (mg/cm^3)	Talbot-XPCI shock speeds for t ≤ 10 ns (km/s)	VISAR shock speed at breakout (km/s)	xRAGE shock speed 3.9 ≤ t ≤ 10 ns (km/s)
20	32.3 ± 1.6	29.67 ± 2.46	23.35
50	26.01 ± 1.6	22.00 ± 1.34	20.99
100	28.10 ± 1.4	17.27 ± 0.95	18.96
250	27.2 ± 1.5	12.91 ± 0.7	16.19
500	14.6 ± 1.2	8.967 ± 1.12	14.49

TABLE III. Aerogel shock speeds U_S using Talbot-XPCI, VISAR, and xRAGE simulations

Density (mg/cm^3)	Talbot-XPCI shock speeds for t ≥ 10 ns (km/s)	VISAR shock speed at breakout (km/s)
17.5	22.30 ± 4.5	19.97 ± 1.51
35	14.81 ± 1.87	16.20 ± 3.4
70	14.16 ± 2.82	15.46± 1.88
105	8.47 ± 1.45	10.07± 1.48

TABLE IV. TPP shock speeds U_S using Talbot-XPCI combined with VISAR breakout times, and VISAR breakout only.

The complementarity of Talbot-XPCI and VISAR measurements becomes evident in Tables III and IV. For the lowest-density aerogel foams (20 mg/cm^3), the estimated shock speed (29.67 ± 2.46) km/s using VISAR breakout times closely matches the shock speed reported by Talbot-XPCI in Figure 4 during the early times (≤ 10 ns) of shock propagation, while the other densities underestimate their speeds. This behavior can be understood[24] by considering that, due to its very low density, this target takes longer to transition from the ballistic to the deceleration phase. As a result, shock breakout occurs while still in the ballistic regime, as the shock has not yet accumulated enough mass behind itself to initiate deceleration. The opposite case occurs in Table IV. Talbot-XPCI data tracked laser-off shock front propagation and therefore VISAR average shock speeds at breakout naturally overestimate Talbot-XPCI shock speeds, except for the lowest density foam that -similarly to the aerogel case- remains in the balistic regime.

IV. DISCUSSION

A. Shock speed scaling in aerogel and TPP foams

The shock velocity trends observed in aerogel and TPP foams follow theoretical predictions but exhibit key differences due to their distinct microstructural characteristics. The average shock speeds over the entire dynamic process are lower in TPP lattice foams compared to aerogel foams at breakout. Moreover, aerogel foams show a best-fit exponent of $\alpha = -0.35 \pm 0.04$, slightly deviating from the theoretical $\rho^{-1/2}$ scaling that assumes full energy conservation in a strong shock regime. In contrast, TPP foams appear to follow $\rho^{-1/2}$ within error bars (see Figure 9).

Note that the VISAR breakout speeds plotted in Figure 9 correspond to an initially supported shock followed by an un-

supported transient once the drive laser turns off. Although one might expect a longer target under identical drive conditions to yield a lower breakout speed and thus making the inferred density scaling law length-dependent, for our 300 and 500 µm aerogel foams the early, supported regime is indistinguishable between 300 and 500 um aerogel of a specific density, i.e. none broke out before laser off. Figure 9 shows that the 300 µm and 500 µm aerogel foams exhibit statistically breakout speeds within statistical/measurement error despite the longer unsupported interval in the 500 um samples. Moreover, Figures 5 and 6 show that although the shock becomes unsupported after 10 ns, there is no abrupt deceleration immediately after laser is turned off; any gradual slowing is most noticeable at densities above 100 mg/cm^3 in both TPP and aerogel foams. Nevertheless, caution is warranted when using breakout speeds for density-scaling studies: they provide a useful late-time benchmark but do not, by themselves, satisfy the assumption of a continuously driven shock, which is why we use Talbot images to provide a more complete picture of shock dynamics.

B. Energy dissipation in aerogel foams and deviation from theoretical scaling

For an ideal strong shock of initial mass density ρ_0, the Rankine-Hugoniot relations predict that shock velocity should scale as $u_s \propto \rho_0^{-1/2}$. Assuming that the shock energy is fully converted into kinetic and internal energy, we can write $E_{shock} = \frac{1}{2}\rho_0 u_s^2 + e_{internal} = E_0$ (constant). For a strong shock, the initial pressure is negligible compared to the shocked pressure, so $P_0 \approx 0$. Therefore, the momentum conservation for the shock jump condition $P - P_0 = \rho_0 u_s u_p$ becomes $P = \rho_0 u_s u_p$. Using the equation of state (EOS) for an ideal gas-like material, we can relate pressure to internal energy using $P = (\gamma - 1)\rho_0 e_{internal}$, where γ is the adiabatic index. Putting together the energy conservation equation $\frac{1}{2}u_p^2 + \frac{P}{(\gamma-1)\rho_0}$=constant with $P = \rho_0 u_s u_p$ gives us $u_s \propto \rho_0^{-1/2}$. We can express the energy flux across the shock front as $E \sim \frac{1}{2}\rho u_s$, where energy flux remains conserved as the shock propagates. Figure 9 suggests aerogel data departing slightly from the $\rho_0^{-1/2}$ and fitting better the curve described by $\propto \rho_0^{-0.29}$, indicating that a fraction of the shock energy is lost e.g. to pore collapse or turbulence, rather than entirely converted to bulk kinetic and thermal energy. We can account for these losses by introducing a density-dependent dissipation term $\varepsilon(\rho_0)$:

$$E_{shock} = E_0 - \varepsilon(\rho_0) \tag{1}$$

where ε represents the energy dissipated per unit mass. Then Equation 1 suggests:

$$u_s^2 \sim \frac{E_0 - \varepsilon(\rho_0)}{\rho_0} \tag{2}$$

$$E_0 - \varepsilon(\rho_0) \propto \rho_0 u_s^2 \propto \rho_0{}^1(\rho_0{}^{-0.35})^2 = \rho_0{}^{1-0.70} = \rho_0{}^{0.30} \tag{3}$$

where we used $u_s \propto \rho_0{}^{-0.35}$ obtained from Figure 9.

Equation 2 suggests that instead of full energy conservation, some fraction $\varepsilon(\rho_0)$ is lost, modifying the available shock energy. Physically, this means that when shock compresses the foam targets, energy is dissipated in the material (e.g. through pore collapse for aerogel foams) and therefore the slight deviation from the expected $\rho_0{}^{1/2}$ scaling as a direct consequence of this energy dissipation mechanism.

C. Influence of Microstructure on Shock Dynamics

The characteristic VISAR imprint of TPP foams (Figure 3) is explained by the high-resolution Talbot-XPCI image maps that show the interaction between the shock front and the lattice, causing not only local inhomogeneities, but also mesoscale effects. The details of this particular dynamic will be discussed in future work, although similar local interactions such as shock–bubble interactions, have been previously modeled and measured by Kurzer-Ogul et al.[57] to study radiation and heat transport. Clearly, TPP shock front evolution differs from those seen in aerogel foams in Figures 2 and 7, confirming that Talbot-XPCI offers an extraordinary platform to look into these local interactions–that control the overall mesoscale shock dynamics–as it provides higher resolution and increased sensitivity to density gradients when compared to standard absorption radiographs.

D. Experimental Benchmarking and Implications

By validating our aerogel foam results against previous studies[24,33,34,36], we establish a benchmark for future shock experiments in low-density TPP foams. While TPP foams have been previously investigated by Dattelbaum et al.[22] using gas-gun-driven plate impact experiments and XPCI, reporting shock speeds of 1.36 km/s for 1.183 g/cm^3, and for densities of 1.178-1.184 g/cm^3 reporting shock speeds of 3.51 - 5.70 km/s[23], our study expands the understanding of TPP foams by exploring densities < 105 mg/cm^3, an unexplored TPP equation-of-state regime under HED drive conditions. Further study has to be done to refine scaling laws for energy dissipation on TPP foams as we report here that they reach lower shock speeds when compared to aerogel foams of similar densities.

Although the laser energy and profile were modeled to match experimental conditions as closely as possible, Figure 7a. and 7b. show a mismatch on the shock front position as a function of time. Limitations in the current CH EOS may cause the simulated CH ablator to deliver less energy density to the foam than occurs experimentally, resulting in underpredicted shock speeds. Alternatively, the energy density may be accurate, but the EOS and opacity models for the foam may underestimate the shock propagation speed. To help distinguish between these possibilities, we show in Fig. 7c the energy density at t=3.9ns, just before the shock enters the foam. This energy density profile provides a quantitative reference

for future comparisons and model validation. Since all aerogel foams used identical ablator stacks, any systematic discrepancy in shock velocity between experiment and simulation is likely attributable to material response models, rather than drive inconsistencies.

V. CONCLUSION AND FUTURE WORK

Our measurements provide the first direct comparison of shock propagation in aerogel versus TPP (two-photon polymerized) foams at densities between 17.5 and 500 mg/cm^3 under HED drive conditions. The structural modulation of the shock front observed in TPP targets highlights the incomplete homogenization of additively manufactured foams at the microscale, particularly when the lattice periodicity is on the order of tens of microns. This anisotropy in shock propagation, which varies with shock orientation relative to lattice geometry, is an important constraint for wetted-foam capsule designs[12] that rely on uniform compression for implosion symmetry. These findings suggest that the lattice scale must be reduced to below several microns to avoid introducing hydrodynamic perturbations or late-time instability seeds as seen in the VISAR breakout imprint and Talbot-XPCI phase contrast images. This is directly relevant to advanced IFE concepts where novel AM foam capsules are being considered[18], and supports ongoing efforts to develop smoother, smaller-pore AM targets.

In addition, we emphasize that the intensity regime studied here ($\sim 10^{13}$ W/cm^2) represents a lower bound for direct-drive IFE concepts. Higher intensities (a few 10^{14} W/cm^2), improved focal spot quality, and smoothing techniques commonly employed in direct drive will likely reduce sensitivity to small-scale inhomogeneities. Nonetheless, our results define a conservative constraint on shock uniformity under moderate drive and provide quantitative inputs for EOS benchmarking, foam selection, and ablator-stack optimization in future capsule design.

The ability to resolve shock front evolution and morphology at these conditions reduces uncertainties in how low-density materials behave during early implosion phases.[18,58] As such, these measurements can now be incorporated into radiation-hydrodynamic codes to refine capsule and ablator configurations across multiple IFE scenarios. As future work, we are pursuing follow-on experiments aimed at reducing density gradient uncertainty from $\sim$ 10-15% (optical methods) to below 5%, thereby enabling proper distinction between various non-local models.[34]

Aerogel and TPP foams exhibit overall shock speed trends consistent with the theoretical $\rho^{-1/2}$ scaling, in agreement with porous material hydrodynamics. For aerogels, we quantified energy dissipation as a function of initial density. In contrast, the limited number of data points and larger uncertainties in the TPP dataset preclude a definitive assessment of dissipation behavior for that class of materials.

xRAGE simulations successfully reproduced the overall shock front morphology observed in Talbot-XPCI experimental images. However, shock velocities were consistently underestimated across all aerogel foam densities. Ongoing simulation efforts aim to investigate the underlying causes of this discrepancy and likely reflects EOS limitations in the ablator and/or foam models.

Future experiments using high-resolution Talbot-XPCI can relax the assumption of constant shock velocity during the laser drive phase and instead resolve instantaneous shock dynamics. Additionally, the spatial resolution demonstrated here opens the possibility of inferring density distributions from deflection data. When combined with shock speed measurements and the Rankine–Hugoniot relations, this approach could enable a fully experimental derivation of the EOS for low-density materials relevant to IFE target design.

ACKNOWLEDGMENTS

This work was funded by the Department of Energy (DOE) Office of Science, Fusion Energy Sciences, under award no. DE-SC 0024882: IFE-STAR issued as SLAC FWP 101126 and FWP100182, DOE National Nuclear Security Administration (NNSA) - High Energy Density Laboratory Plasmas Grant DE-NA0004028 and NNSA Stewardship Science Academic Programs under DOE Cooperative Agreement DE-NA0004148, and Los Alamos National Laboratory, operated by Triad National Security, LLC, for the NNSA - DOE Contract No. 89233218CNA000001.

The use of the Linac Coherent Light Source (LCLS), SLAC National Accelerator Laboratory, is supported by the U.S. Department of Energy, Office of Science, Office of Basic Energy Sciences under Contract No. DE-AC02-76SF00515. The MEC instrument is supported also by the U.S. Department of Energy Office of Science, Fusion Energy Science under Contract No. DE-AC02-76SF00515, FWP 100106.

Funding and support to develop and benchmark the TIA/TNT code was provided by Research Grant No. PID2022-137632OB-I00 from the Spanish Ministry of Science and Innovation. This work has also been carried out within the framework of the EUROfusion consortium, funded by the European Union via the Euratom Research and Training Program (Grant Agreement Nos. 633053 and 101052200—EUROfusion). The views and opinions expressed are, however, those of the author(s) only and do not necessarily reflect those of the European Union or the European Commission. Neither the European Union nor the European Commission can be held responsible for them. The involved teams have operated within the framework of the Enabling Research Projects: Grant number AWP21-ENR-IFE.01.CEA.

C.P., D.E. and A.K. acknowledge support from DOE, Office of Science, Fusion Energy Sciences, under award no. DE-SC 0023475. L.I. acknowledges support from the Agencia Nacional de Investigacion y Desarrollo (ANID), Subdirección de Capital Humano, Doctorado Nacional grant 2023-21230431, from the Chilean government. W.M.M. acknowledges support from the National Science Foundation Graduate Research Fellowship Program under Grant No. DGE-2146755. D.M. acknowledges the funding from Hellenic Mediterranean Uni-

version within the project "Proposal for post-doctoral research at the Institute of Plasma Physics and Lasers (IPPL) of Hellenic Mediterranean University (HMU)" in the context of the 2607/Φ.120/04-05-2022 call of HMU for post-doctoral research. D.M. acknowledge financial support from the French government in the framework of the University of Bordeaux's France 2030 program / GPR LIGHT.

AUTHOR DECLARATIONS

The authors have no conflicts to disclose.

DATA AVAILABILITY STATEMENT

The data that support the findings of this study are available from the corresponding author upon reasonable request.

REFERENCES

[1]A. Zylstra, O. Hurricane, D. Callahan, A. Kritcher, J. Ralph, H. Robey, J. Ross, C. Young, K. Baker, D. Casey, *et al.*, "Burning plasma achieved in inertial fusion," Nature **601**, 542–548 (2022).
[2]H. Abu-Shawareb, R. Acree, P. Adams, J. Adams, B. Addis, R. Aden, P. Adrian, B. Afeyan, M. Aggleton, L. Aghaian, *et al.*, "Lawson criterion for ignition exceeded in an inertial fusion experiment," Physical review letters **129**, 075001 (2022).
[3]O. A. Hurricane, "How ignition and target gain> 1 were achieved in inertial fusion," High Energy Density Physics **53**, 101157 (2024).
[4]H. Abu-Shawareb, R. Acree, P. Adams, J. Adams, B. Addis, R. Aden, P. Adrian, B. Afeyan, M. Aggleton, L. Aghaian, *et al.*, "Achievement of target gain larger than unity in an inertial fusion experiment," Physical Review Letters **132**, 065102 (2024).
[5]T. Ma, D. Mariscal, R. Anirudh, T. Bremer, B. Djordjevic, T. Galvin, E. Grace, S. Herriot, S. Jacobs, B. Kailkhura, *et al.*, "Accelerating the rate of discovery: Toward high-repetition-rate hed science," Plasma Physics and Controlled Fusion **63**, 104003 (2021).
[6]I. Prencipe, J. Fuchs, S. Pascarelli, D. Schumacher, R. Stephens, N. Alexander, R. Briggs, M. Büscher, M. Cernaianu, A. Choukourov, *et al.*, "Targets for high repetition rate laser facilities: needs, challenges and perspectives," High Power Laser Science and Engineering **5**, e17 (2017).
[7]J. Nuckolls, L. Wood, A. Thiessen, and G. Zimmerman, "Laser compression of matter to super-high densities: Thermonuclear (ctr) applications," Nature **239**, 139–142 (1972).
[8]M. Dunne, E. Moses, P. Amendt, T. Anklam, A. Bayramian, E. Bliss, B. Debs, R. Deri, T. D. d. l. Rubia, B. El-Dasher, *et al.*, "Timely delivery of laser inertial fusion energy (life)," Fusion Science and Technology **60**, 19–27 (2011).
[9]B. M. Haines, T. J. Murphy, R. E. Olson, Y. Kim, B. J. Albright, B. Appelbe, T. H. Day, M. A. Gunderson, C. E. Hamilton, T. Morrow, and B. M. Patterson, "The dynamics, mixing, and thermonuclear burn of compressed foams with varied gas fills," Physics of Plasmas **30**, 072705 (2023), https://pubs.aip.org/aip/pop/article-pdf/doi/10.1063/5.0154600/18042484/072705_1_5.0154600.pdf.
[10]S. E. Bodner, A. J. Schmitt, and J. D. Sethian, "Laser requirements for a laser fusion energy power plant," High Power Laser Science and Engineering **1**, 2–10 (2013).
[11]A. Lucianetti, M. Sawicka, O. Slezak, M. Divoky, J. Pilar, V. Jambunathan, S. Bonora, R. Antipenkov, and T. Mocek, "Design of a kj-class hilase laser as a driver for inertial fusion energy," High Power Laser Science and Engineering **2**, e13 (2014).
[12]R. Olson, M. Schmitt, B. Haines, G. Kemp, C. Yeamans, B. Blue, D. Schmidt, A. Haid, M. Farrell, P. Bradley, *et al.*, "A polar direct drive liquid deuterium–tritium wetted foam target concept for inertial confinement fusion," Physics of Plasmas **28** (2021).
[13]R. Sacks and D. Darling, "Direct drive cryogenic icf capsules employing dt wetted foam," Nuclear Fusion **27**, 447 (1987).
[14]K. Nagai, C. S. A. Musgrave, and W. Nazarov, "A review of low density porous materials used in laser plasma experiments," Physics of Plasmas **25**, 030501 (2018), https://pubs.aip.org/aip/pop/article-pdf/doi/10.1063/1.5009689/19763539/030501_1_online.pdf.
[15]G. Kemp, C. Yeamans, M. Hohenberger, S. Bhandarkar, B. Blue, T. Briggs, R. Craxton, L. Divol, M. Do, M. Farrell, *et al.*, "Exploration of polar direct drive wetted foam concepts for neutron sources on the national ignition facility laser," Physics of Plasmas **32** (2025).
[16]S. Kawata, H.-B. Sun, T. Tanaka, and K. Takada, "Finer features for functional microdevices," Nature **412**, 697–698 (2001).
[17]J. S. Oakdale, R. F. Smith, J.-B. Forien, W. L. Smith, S. J. Ali, L. B. Bayu Aji, T. M. Willey, J. Ye, A. W. van Buuren, M. A. Worthington, *et al.*, "Direct laser writing of low-density interdigitated foams for plasma drive shaping," Advanced Functional Materials **27**, 1702425 (2017).
[18]J. Milovich, O. Jones, R. Berger, G. Kemp, J. Oakdale, J. Biener, M. Belyaev, D. Mariscal, S. Langer, P. Sterne, *et al.*, "Simulation studies of the interaction of laser radiation with additively manufactured foams," Plasma Physics and Controlled Fusion **63**, 055009 (2021).
[19]D. Mariscal, O. Jones, R. Berger, S. Patankar, K. Baker, T. Baumann, M. Biener, C. Goyon, B. Pollock, J. Moody, *et al.*, "Laser transport and backscatter in low-density sio2 and ta2o5 foams," Physics of Plasmas **28** (2021).
[20]S. K. Saha, D. Wang, V. H. Nguyen, Y. Chang, J. S. Oakdale, and S.-C. Chen, "Scalable submicrometer additive manufacturing," Science **366**, 105–109 (2019).
[21]J. Limpouch, V. Tikhonchuk, O. Renner, S. Agarwal, T. Burian, J. Červenka, J. Dostál, R. Dudžák, D. Ettel, A. Gintrand, *et al.*, "Laser interaction with undercritical foams of different spatial structures," Matter and Radiation at Extremes **10** (2025).
[22]D. M. Dattelbaum, A. Ionita, B. M. Patterson, B. A. Branch, and L. Kuettner, "Shockwave dissipation by interface-dominated porous structures," AIP Advances **10** (2020).
[23]D. Dattelbaum, B. Branch, A. Ionita, B. Patterson, L. Kuettner, and M. Herman, "Shockwave interactions with additively-manufactured polymer structures," in *AIP Conference Proceedings*, Vol. 2272 (AIP Publishing, 2020).
[24]G. Rigon, B. Albertazzi, P. Mabey, T. Michel, E. Falize, V. Bouffetier, L. Ceurvorst, L. Masse, M. Koenig, and A. Casner, "Exploring the atwood-number dependence of the highly nonlinear rayleigh-taylor instability regime in high-energy-density conditions," Physical Review E **104**, 045213 (2021).
[25]M. Koenig, A. Benuzzi, F. Philippe, D. Batani, T. Hall, N. Grandjouan, and W. Nazarov, "Equation of state data experiments for plastic foams using smoothed laser beams," Physics of plasmas **6**, 3296–3301 (1999).
[26]M. Knudson and R. Lemke, "Shock response of low-density silica aerogel in the multi-mbar regime," Journal of Applied Physics **114** (2013).
[27]S. Y. Gus' kov and R. Yakhin, "Equation of state of a partially homogenized plasma of low-dense porous matter," Physics of Plasmas **30** (2023).
[28]R. Dezulian, F. Canova, S. Barbanotti, F. Orsenigo, R. Redaelli, T. Vinci, G. Lucchini, D. Batani, B. Rus, J. Polan, *et al.*, "Equation of state data of plastic foams at mbar pressures," in *Frontiers of plasma physics and technology. Proceedings of an international conference* (2008).
[29]K. Falk, C. McCoy, C. L. Fryer, C. W. Greeff, A. L. Hungerford, D. Montgomery, D. W. Schmidt, D. G. Sheppard, J. R. Williams, T. R. Boehly, *et al.*, "Temperature measurements of shocked silica aerogel foam," Physical Review E **90**, 033107 (2014).
[30]N. C. Holmes, "Shock compression of low-density foams," in *AIP Conference Proceedings*, Vol. 309 (American Institute of Physics, 1994) pp. 153–156.
[31]D. M. Dattelbaum and J. D. Coe, "Shock-driven decomposition of polymers and polymeric foams," Polymers **11**, 493 (2019).
[32]D. Batani, R. Dezulian, R. Redaelli, R. Benocci, H. Stabile, F. Canova, T. Desai, G. Lucchini, E. Krousky, K. Masek, *et al.*, "Recent experiments on the hydrodynamics of laser-produced plasmas conducted at the pals laboratory," Laser and Particle Beams **25**, 127–141 (2007).
[33]L. Antonelli, W. Theobald, F. Barbato, S. Atzeni, D. Batani, R. Betti, V. Bouffetier, A. Casner, L. Ceurvorst, D. Cao, J. J. Ruby, K. Glize,

T. Goudal, A. Kar, M. Khan, A. Dearling, M. Koenig, P. M. Nilson, R. H. H. Scott, O. Turianska, M. Wei, and N. C. Woolsey, "X-ray phase-contrast imaging of strong shocks on omega ep," Review of Scientific Instruments **95**, 113504 (2024), https://pubs.aip.org/aip/rsi/article-pdf/doi/10.1063/5.0168059/20242066/113504_1_5.0168059.pdf.

[34]Y. Aglitskiy, A. Velikovich, M. Karasik, A. Schmitt, V. Serlin, J. Weaver, J. Oh, S. Obenschain, and K. Cochrane, "Absolute hugoniot measurements for ch foams in the 2–9 mbar range," Physics of Plasmas **25** (2018).

[35]D. M. Dattelbaum, B. C. MacNider, R. C. Huber, and J. M. Lang, "Shock compression of a low-density carbon foam," Materials Letters **360**, 135991 (2024).

[36]K. A. Maerzke, J. D. Coe, D. A. Fredenburg, J. M. Lang, and D. M. Dattelbaum, "Equations of state and shock-driven chemistry in poly (dimethylsiloxane)-based foams," in *AIP Conference Proceedings*, Vol. 1979 (AIP Publishing, 2018).

[37]G. Pérez-Callejo, V. Bouffetier, L. Ceurvorst, T. Goudal, S. R. Klein, D. Svyatskiy, M. Holec, P. Perez-Martin, K. Falk, A. Casner, T. E. Weber, G. Kagan, and M. P. Valdivia, "Phase imaging of irradiated foils at the omega ep facility using phase-stepping x-ray talbot–lau deflectometry," High Power Laser Science and Engineering **11**, e49 (2023).

[38]B. Nagler, B. Arnold, G. Bouchard, R. F. Boyce, R. M. Boyce, A. Callen, M. Campell, R. Curiel, E. Galtier, J. Garofoli, E. Granados, J. Hastings, G. Hays, P. Heimann, R. W. Lee, D. Milathianaki, L. Plummer, A. Schropp, A. Wallace, M. Welch, W. White, Z. Xing, J. Yin, J. Young, U. Zastrau, and H. J. Lee, "The matter in extreme conditions instrument at the linac coherent light source," Synchrotron Radiation **22**, 520–525 (2015).

[39]A. Schropp, R. Hoppe, V. Meier, J. Patommel, F. Seiboth, Y. Ping, D. G. Hicks, M. A. Beckwith, G. W. Collins, A. Higginbotham, *et al.*, "Imaging shock waves in diamond with both high temporal and spatial resolution at an xfel," Scientific reports **5**, 11089 (2015).

[40]G. Rigon, B. Albertazzi, T. Pikuz, P. Mabey, V. Bouffetier, N. Ozaki, T. Vinci, F. Barbato, E. Falize, Y. Inubushi, *et al.*, "Micron-scale phenomena observed in a turbulent laser-produced plasma," Nature communications **12**, 2679 (2021).

[41]D. S. Montgomery, "Invited article: X-ray phase contrast imaging in inertial confinement fusion and high energy density research," Review of Scientific Instruments **94** (2023).

[42]A. Olivo and E. Castelli, "X-ray phase contrast imaging: From synchrotrons to conventional sources," La rivista del nuovo cimento **37**, 467–508 (2014).

[43]L. Antonelli, S. Atzeni, A. Schiavi, S. Baton, E. Brambrink, M. Koenig, C. Rousseaux, M. Richetta, D. Batani, P. Forestier-Colleoni, *et al.*, "Laser-driven shock waves studied by x-ray radiography," Physical Review E **95**, 063205 (2017).

[44]R. Cauble, T. Perry, D. Bach, K. Budil, B. Hammel, G. Collins, D. Gold, J. Dunn, P. Celliers, L. Da Silva, *et al.*, "Absolute equation-of-state data in the 10–40 mbar (1–4 tpa) regime," Physical review letters **80**, 1248 (1998).

[45]F. Marshall, P. McKenty, J. Delettrez, R. Epstein, J. Knauer, V. Smalyuk, J. Frenje, C. Li, R. Petrasso, F. Séguin, *et al.*, "Plasma-density determination from x-ray radiography of laser-driven spherical implosions," Physical review letters **102**, 185004 (2009).

[46]D. C. Swift, A. L. Kritcher, J. A. Hawreliak, A. Lazicki, A. MacPhee, B. Bachmann, T. Döppner, J. Nilsen, G. W. Collins, S. Glenzer, *et al.*, "Absolute hugoniot measurements from a spherically convergent shock using x-ray radiography," Review of Scientific Instruments **89** (2018).

[47]L. Ceurvorst, W. Theobald, M. Rosenberg, P. Radha, C. Stoeckl, R. Betti, K. Anderson, J. Marozas, V. Goncharov, E. Campbell, *et al.*, "Development of an x-ray radiography platform to study laser-direct-drive energy coupling at the national ignition facility," Review of Scientific Instruments **93** (2022).

[48]M. Valdivia, D. Stutman, C. Stoeckl, W. Theobald, G. Collins, V. Bouffetier, M. Vescovi, C. Mileham, I. Begishev, S. Klein, *et al.*, "Talbot-lau x-ray deflectometer: Refraction-based hedp imaging diagnostic," Review of Scientific Instruments **92** (2021).

[49]M. Valdivia, G. Perez-Callejo, G. Collins, C. Stoeckl, T. Filkins, C. Mileham, M. Romanofsky, I. Begishev, W. Theobald, *et al.*, "Current advances on talbot–lau x-ray imaging diagnostics for high energy density experiments," Review of Scientific Instruments **93** (2022).

[50]V. Bouffetier, G. Pérez-Callejo, D. Stutman, C. Stoeckl, I. Begishev, W. Theobald, T. Filkins, C. Mileham, L. Ceurvorst, S. Klein, *et al.*, "Referenceless, grating-based, single shot x-ray phase contrast imaging with optimized laser-driven k-α sources," Optics Express **32**, 34694–34709 (2024).

[51]B. Nagler, A. Schropp, E. C. Galtier, B. Arnold, S. B. Brown, A. Fry, A. Gleason, E. Granados, A. Hashim, J. B. Hastings, D. Samberg, F. Seiboth, F. Tavella, Z. Xing, H. J. Lee, and C. G. Schroer, "The phase-contrast imaging instrument at the matter in extreme conditions endstation at lcls," Review of Scientific Instruments **87** (2016).

[52]E. Galtier, H. J. Lee, D. Khaghani, N. Boiadjieva, P. McGehee, A. Arnott, B. Arnold, M. Berboucha, E. Cunningham, N. Czapla, G. Dyer, R. Ettelbrick, P. Hart, P. Heimann, M. Welch, M. Makita, A. E. Gleason, S. Pandolfi, A. Sakdinawat, Y. Liu, M. J. Wojcik, D. Hodge, R. Sandberg, M. P. Valdivia, V. Bouffetier, G. Pérez-Callejo, F. Seiboth, and B. Nagler, "X-ray microscopy and talbot imaging with the matter in extreme conditions x-ray imager at lcls," Scientific Reports **15** (2025).

[53]G. Pérez-Callejo, V. Bouffetier, L. Ceurvorst, T. Goudal, M. Valdivia, D. Stutman, and A. Casner, "TIA: A forward model and analyzer for Talbot interferometry experiments of dense plasmas," Physics of Plasmas **29**, 043901 (2022).

[54]M. P. Valdivia, G. Pérez-Callejo, L. Izquierdo, F. Veloso, A. Truong, H. Hu, N. Dilworth, S. C. Bott-Suzuki, and V. Bouffetier, "z-pinch interferometry analysis with the fourier-based tnt code," IEEE Transactions on Plasma Science (2024).

[55]P. M. Celliers and M. Millot, "Imaging velocity interferometer system for any reflector (visar) diagnostics for high energy density sciences," Review of Scientific Instruments **94** (2023).

[56]A. Kar, T. Boehly, P. Radha, D. Edgell, S. Hu, P. Nilson, A. Shvydky, W. Theobald, D. Cao, K. Anderson, *et al.*, "Simulated refraction-enhanced x-ray radiography of laser-driven shocks," Physics of Plasmas **26** (2019).

[57]K. Kurzer-Ogul, B. M. Haines, D. S. Montgomery, S. Pandolfi, J. P. Sauppe, A. F. Leong, D. Hodge, P. M. Kozlowski, S. Marchesini, E. Cunningham, *et al.*, "Radiation and heat transport in divergent shock–bubble interactions," Physics of Plasmas **31** (2024).

[58]S. X. Hu, W. Theobald, P. B. Radha, J. L. Peebles, S. P. Regan, A. Nikroo, M. J. Bonino, D. R. Harding, V. N. Goncharov, N. Petta, T. C. Sangster, and E. M. Campbell, "Mitigating laser-imprint effects in direct-drive inertial confinement fusion implosions with an above-critical-density foam layer," Physics of Plasmas **25**, 082710 (2018), https://pubs.aip.org/aip/pop/article-pdf/doi/10.1063/1.5044609/15802972/082710_1_online.pdf.